Strategic Astrophysics Technology

Technology Milestone White Paper

Technology development in UV coronagraphy to enable characterization of Earth-like exoplanets

Kyle Van Gorkom, Ewan S. Douglas, Ramya M. Anche,
Christopher B. Mendillo, Jessica Gersh-Range, Tyler Robinson,
Justin Hom, Bruce Macintosh, Nikole Lewis, Mamadou N'Diaye

April 7, 2025

Prepared By:

E-SIGNED by Kyle Van Gorkom
on 2025-04-08 00:06:02 GMT

Kyle Van Gorkom
Principal Investigator
University of Arizona

Date

Approved By:

E-SIGNED by Brendan Crill
on 2025-04-08 00:00:11 GMT

Brendan Crill
ExEP Deputy Program Chief Technologist

Date

E-SIGNED by Nicholas Siegler
on 2025-04-08 01:47:49 GMT

Nick Siegler
ExEP Program Chief Technologist

Date

E-SIGNED by Lucas Paganini
on 2025-04-08 13:20:46 GMT

Lucas Paganini
ExEP Program Executive, NASA-HQ

Date

1 Table of Contents

2 Objective

NASA's Habitable Worlds Observatory (HWO) concept and the 2020 Decadal Survey's recommendation to develop a large space telescope to "detect and characterize Earth-like extrasolar planets" requires new starlight suppression technologies to probe a variety of biomarkers across multiple wavelengths. Oxygen abundance in an exoplanet atmosphere is one of the key ensembles of features which suggest biological activity and constrains the evolutionary stage of an Earth-like planet atmosphere (Archean, Protozoic, or Modern Earth)[1]. On Earth-like planets, ozone generated by a combination of photolysed atomic oxygen with molecular oxygen is unlikely to persist without a biological source when accompanied by methane (CH4). Broadband absorption due to ozone is a dramatic signal, starting shortward of 350 nm and peaking below 300 nm, which can be detected with low spectral resolution. Longer blue and violet light also probes Rayleigh scattering effects, constraining atmospheric mean molecular mass. Despite the high value of direct ultraviolet (UV) exoplanet observations, high-contrast coronagraph demonstrations have yet to be performed in the UV. The shortest wavelength probed by the Roman Coronagraph technology demonstration mission is 545 nm, and current high contrast imaging testbeds probe a similar (or longer) wavelength regime, leaving a considerable technology gap at shorter wavelengths.

Typical coronagraph leakage sources such as wavefront error, surface scatter, polarization aberrations, and coronagraph mask quality all become more significant in the UV and threaten the viability of HWO to produce meaningful science in this vital regime. Establishing the technological feasibility of measuring UV ozone absorption as a means of characterizing Earth-like planets is thus a key step to designing the HWO. This effort seeks to lay the groundwork for such a design by developing detailed contrast budgets for UV coronagraphy and validating them in a vacuum environment. The results will be used to guide the development of optical requirements for HWO to enable its science goals.

The four major objectives of this effort are:

1. Development of detailed analytic and numerical models to produce a contrast budget and integrated performance prediction for (a) the as-built Space Coronagraph Optical Bench (SCoOB) testbed and (b) a notional UV coronagraph instrument with a segmented aperture that closes at the 10^{-10} contrast level for comparison to HWO needs.

2. Component-level metrology of as-built optics, coronagraph masks, and deformable mirrors (high-resolution surface roughness metrology, scattered light measurements, and Mueller matrix spectropolarimetry). This effort updates the testbed contrast budget with measured values at scales required for UV performance, serves as a cross-check of assumptions in a general budget, and could identify areas where current state-of-the-art fabrication techniques fall short of the requirements for UV coronagraphy.

3. Demonstration of high contrast imaging at UV wavelengths on a testbed in a vacuum environment. This effort validates the modeling effort that produces the contrast budget and the integration of component metrology into that model. To aid in disentangling architecture- and wavelength-specific effects, the project will simultaneously explore two complementary coronagraph designs: a vector vortex coronagraph

(VVC)[2–6] and a shaped pupil coronagraph (SPC)[7–9].

4. Predictions of science yield informed by contrast performance and UV coverage. An outcome of this effort is the suggestion of requirements for UV high-contrast imaging and polarimetry, including additional exoplanet science cases in blue and UV wavelengths, such as Rayleigh scattering in extrasolar terrestrial and gas giant atmospheres and excess UV emission generated from actively-accreting protoplanets

3 Background

3.1 Expected Significance

This project addresses a technology gap for one of the highest-priority mission recommendations of *Astro2020* Decadal Survey, the Habitable Worlds Observatory (HWO). In the 2024 Astrophysics Strategic Technology Gap list, "Coronagraph Contrast and Efficiency in the Near Ultraviolet" is considered a highest-priority Tier 1 gap [10], and this project aims to be the first to address this gap. Strategic Objective 1.2 of the 2022 NASA Strategic Plan lists the detection and characterization of habitable exoplanets under the sub-category "Searching for Life Elsewhere" [11].

With respect to UV coronagraphy in particular, Section 4.2 of the Exoplanet Exploration Program's *Progress in Technology for Exoplanet Missions* states, "Measuring broad atmospheric features in the near ultraviolet (UV) band is necessary for spectral characterization of terrestrial planets exoplanets." [12] The UV spectral range provides crucial access to ozone spectral features for oxygenated atmospheres [13]. Ozone is photochemically produced in oxygen-bearing atmospheres and, thus, is a classic biosignature. Critically, the ozone Hartley (200–310 nm) and Huggins (310–350 nm) bands can indicate the presence of molecular oxygen even in weakly oxygenated atmospheres due to the non-linear relationship between ozone and oxygen concentrations [14].

UV coronagraphy also has applications in the observation and characterization of actively-accreting protoplanets and their circumplanetary disks (CPDs) [15]. Few observations of these systems in the UV have been performed, with the only clear detection being PDS 70 b at 336 nm using HST-WFC3 without a coronagraph [16]. Non-detections are likely contrast-limited, with WFC3 only achieving a $\sim 10^{-4}$ contrast at $< 1''$ without the use of a coronagraph. The *Astro2020* Decadal Survey states that obtaining high spatial and low spectral resolution of CPDs will provide crucial insights on protoplanet masses, accretion rates, and planetary formation mechanisms.

Section 2.1 of the *Progress in Technology for Exoplanet Missions* document calls out ultraviolet coronagraphy down to 200 nm as an area in need of "detailed study," as it represents a 2x shorter wavelength compared to state-of-the-art laboratory demonstrations and is expected to bring challenges in "the areas of polarization aberrations, reflectivity/scattering, contamination issues, and wavefront control" [12]. The Roman Coronagraph Instrument will validate a detailed contrast budget and modeling effort [17] for a high contrast imaging instrument on a space telescope, but it is a technology demonstrator required only to reach 10^{-7} contrast, and, more significantly, its wavelength coverages reaches only as short as 545 nm [18].

Although exoplanet direct imaging coronagraphy in the UV has not been demonstrated in a laboratory setting at any contrast level (to our knowledge), contrast performance should scale predictably as a function of wavelength (for example, see [19] for the scaling law of Talbot-limited contrast as a function of central wavelength and bandwidth). Visible coronagraphy for exoplanet imaging at the $<10^{-8}$ raw contrast level is TRL 6 (see [20], for example), and scaling laws that extend performance to UV wavelengths serve as a "proof of concept" for the feasibility of coronagraphy at UV wavelengths, indicating a TRL 3 rating. By developing analytical and numerical performance predictions and validating these predictions with a demonstration of UV coronagraphy in a vacuum testbed, this project aims to advance UV coronagraphy from TRL 3 to TRL 4.

3.2 The challenge of coronagraphy in the UV

Extending coronagraphy from visible down to UV wavelengths at the contrast levels required by HWO brings with it a number of challenges in the areas of optical coatings, control of polarization aberrations, wavefront sensing and control (both in terms of tighter requirements and fewer photons available for sensing), and contamination and scattered light control. A number of these challenges are identified in recent white papers[21] and the final report of the Coronagraph Technology Roadmap Working Group[22]. A selection of the terms expected to dominate the contrast budget are given in Table 1 and are described in more detail below, focusing in particular on the terms expected to limit contrast performance in the context of a coronagraph testbed. In the following discussion, we define contrast as $C = I_{\text{speckle}}/I_{\text{PSF}}$, the ratio of the uncorrected speckles in the dark hole to the peak of the non-coronagraphic PSF. The content below summarizes a similar discussion in Van Gorkom et al. 2025[23].

3.2.1 Polarization aberrations

Polarization aberrations are the polarization-dependent amplitude and phase aberrations that arise in any optical system from Fresnel reflection and transmission coefficients at each surface in an instrument's optical train[24, 37]. Polarization aberrations can be described by diattenuation (amplitude aberrations) and retardance (phase aberrations). As these aberrations occur in orthogonal polarization states, a deformable mirror cannot completely correct these aberrations simultaneously in both polarizations. The residual polarization aberrations leak through the coronagraph, creating polarization-dependent speckles in the focal plane that limit the contrast in a high contrast imaging instrument. Further, these polarization aberrations are wavelength-dependent and directly related to refractive index of the coatings in a system comprised primary of reflective optics. As most coatings are optimized for better throughput in visible wavelengths, they have been found to show higher polarization aberrations at UV wavelengths.

3.2.2 Surface and reflectivity errors

Phase and amplitude errors in the wavefront propagated through the coronagraph system create leakage through the coronagraph mask and appear as speckles in the focal plane at locations determined by the spatial frequency content of the errors. Assuming a coronagraph

Term	Summary	References
Polarization Aberrations	Orthogonal polarization states pick up non-common aberrations from telescope and instrument optics that can only be partially corrected	[24–26]
Surface Errors	Speckles from static aberration modes not rejected by coronagraph optics; out-of-pupil phase errors are mapped via the Talbot effect into chromatic amplitude aberrations	[19]
Surface Roughness	Surface errors and particulate contamination at spatial frequencies too high to be captured in a numerical diffraction propagation model; independent scattering model in tools like FRED or a bi-directional scattering distribution function simulation	[17, 27]
DM Quantization	Bit depth of DM electronics results in a minimum step size in actuator motion	[28]
DM Stability	Long-term drift (creep, for example) and high-frequency dynamics from sources like electronics noise	[29, 30]
WFE Stability	Drift in WFE due to thermal and inertial disturbances in the telescope and instrument; tailored solution requires a STOP model and control residuals, but a general treatment can bound the performance with a parameterized power spectrum approach	[31]
Jitter	High-frequency line-of-sight error that can cause stellar leakage through coronagraph mask	[32, 33]
Mask Fabrication	Fabrication deviations from mask designs; e.g., finite pixel resolution in SPC fabrication or variations in retardance and fast axis in VVC fabrication	[34]
Coating Errors	Variations in coating thickness across optical surfaces create amplitude and polarization aberrations	[35]
Beamwalk	Line-of-sight jitter upstream of the fast steering mirror (FSM) causes beam translation on optic surfaces, resulting in dynamic, high spatial-frequency aberrations	[27]
Optical ghosts	Back reflections from transmissive optics result in incoherent speckles in the focal plane	[36]

Table 1: *Primary terms to be included in the contrast budget effort. The magnitudes of the individual terms are coronagraph-, wavelength-, bandwidth-, and instrument-dependent.*

that perfectly removes the on-axis Airy pattern, the contrast contributed by an uncorrected sinusoidal pupil-plane phase aberration of amplitude α with a spatial frequency of n cycles per aperture D in a bandwidth $B = \Delta\lambda/\lambda_0$ at central wavelength λ_0 is approximately

$$C \approx \alpha^2 \frac{4\pi^2}{\lambda_0^2} \left[\frac{1}{1 - \left(\frac{B}{2}\right)^2} \right] \tag{1}$$

at the $\pm n\lambda_0/D$ separation in the focal plane. In the absence of wavefront correction, pupil-plane aberrations contribute a contrast term that scales as λ_0^{-2}.

Wavefront errors typically arise from uncorrected figure and reflectivity errors on optical surfaces in the coronagraph instrument, most of which are located in planes that are not conjugate to the pupil. The wavefront aberrations induced by these surfaces cycle chromatically between phase and amplitude at propagation distances characterized by the Talbot length

$$z_T = \frac{2}{\lambda(n/D)^2}. \tag{2}$$

The chromaticity of this phase-amplitude mixing limits the contrast as a function of the bandwidth[19, 38, 39]. The λ^{-1} dependence in the Talbot length implies weaker chromatic phase-amplitude mixing in the UV compared to visible. To the first-order, however, the post-control contrast floor with a single DM targeting a half-sided dark hole (DH) depends only on the bandwidth and not the central wavelength[19]. The contrast residual due to higher order terms (e.g., second-order phase and frequency-folding[40]) does show a strong dependence on the central wavelength. This contrast floor is dominated by a λ_0^{-4} term and implies a 16× larger contribution to the overall contrast at 300 nm compared to 600 nm.

3.2.3 Scattering and contamination

Scattered light in a coronagraph system creates an incoherent contrast floor and arises from a combination of defects in the focal plane mask[41], scratches and dust particles on optical surfaces[42, 43], and surface roughness of the reflective optics[44–52]. Scattering due to optical surface roughness can be quantified in terms of the bidirectional scattering distribution function (BSDF), defined in terms of the surface power spectral density (PSD)

$$BSDF = \frac{16\pi^2}{\lambda^4} cos(\theta_i) cos(\theta_s) PSD, \tag{3}$$

where λ is the wavelength of light, θ_i is the incident ray angle, and θ_s is the ray scattering angle. The BSDF has a strong λ^{-4} dependence on wavelength, which implies that the scattered light background is 16× larger at 300 nm than at 600 nm.

Particulate contamination can be another significant source of scattering. Dust on the HST primary mirror was modeled as a population of absorbers that diffractively scattered light to the wings of the PSF[53]. Performance simulations for the Gemini Planet Imager (GPI) modeled dust as pixel-scale amplitude defects on each surface in a diffraction simulation to produce contrast predictions as a function of cleanliness level[54], although this analysis was limited to a central wavelength of 1.65 µm and $\sim 10^{-7}$ contrast levels. More modeling is needed to understand the requirements on contamination control for high contrast imaging at 10^{-10} contrast in the UV[21, 22].

3.2.4 Deformable mirror electronics

The quantization of the commands sent to the deformable mirror (DM) actuators to the least significant bit (LSB) of the DM electronics sets a minimum actuator step size, which limits the achievable contrast. For a Kilo-C MEMS device from Boston Micromachines Corp. (BMC), the contrast floor due to this effect is given by[28]

$$C_{\text{quantization}}(\alpha) = \frac{16\pi}{3n_{\text{act}}^2}\left(\frac{h_{\text{min}}}{\lambda}\right)^2 \pi^2\omega^4 e^{-(\alpha/\alpha_{\text{infl}})^2}, \tag{4}$$

where α is the angular separation in the focal plane, n_{act} is the number of actuators across the pupil (after the Lyot stop), h_{min} is the minimum actuator step size, $\omega = d/p$ is the ratio of the Gaussian influence function radius d to the actuator pitch p, and $\alpha_{\text{inf}} = \frac{\sqrt{2}\lambda}{2\pi d}$.

High-frequency noise on each actuator (due to voltage noise from the electronics, for example), can limit the contrast in a similar fashion:

$$C_{\text{noise}}(\alpha) = 64\frac{\pi}{n_{\text{act}}^2}\left(\frac{h_{\text{noise}}}{\lambda}\right)^2 \pi^2\omega^4 e^{-(\alpha/\alpha_{\text{infl}})^2}, \tag{5}$$

where h_{noise} is the RMS actuator motion due to an independent Gaussian noise on each actuator. In both cases, the small-separation contrast $C \propto \lambda^{-2}$. The DM electronics for a coronagraph operating at 300 nm will require 4× lower quantization limit and noise compared to 600 nm to achieve equivalent performance.

3.2.5 Jitter and beam walk

High temporal frequency line-of-sight error, either telescope pointing error or instrument-level vibrations, can create incoherent leakage through the coronagraph. The coronagraph architecture strongly dictates sensitivity to this effect—a vector vortex coronagraph (VVC)[2–6] with a higher charge, for example, can largely mitigate sensitivity to jitter, and pupil-plane masks are generally insensitive.

Beam walk[27, 55], the translation or shear of the beam footprint on surfaces in the optical train, is a second-order term that arises from jitter. Beam walk generates dynamic high spatial frequency content in the wavefront error seen by the coronagraph and is largely independent of the coronagraph architecture. A jitter or low-order wavefront sensing (LOWFS) loop can mitigate this term, but beam walk will still be present on surfaces upstream of the fast steering mirror (FSM). Beam walk on a single optical surface with a surface error of amplitude α at n/D cycles/aperture at a distance z from the pupil (assumed here to be conjugate to the jitter source) generates an incoherent contrast given by[23]

$$C_{\text{beamwalk}} = \alpha^2\frac{2\pi^2}{\lambda^2}\left[1 - e^{-2\pi^2\left(z\frac{n}{D}\sigma\right)^2}\right] \approx \alpha^2\frac{4\pi^4}{\lambda^2}z^2\left(\frac{n}{D}\right)^2\sigma^2, \tag{6}$$

where σ is the RMS jitter (in radians). The λ^{-2} dependence implies a 4× stricter requirement on jitter due to beam walk at 300 nm vs 600 nm.

3.2.6 Separation angles

A factor that can moderate the above challenges faced in pushing high contrast imaging into the UV is the scaling of separation angle in terms of angular resolution element λ/D. A fixed on-sky angular separation at 600 nm corresponds to a 3× larger separation in λ/D at 200 nm. This increased angular resolution moderates sensitivity to the contrast-limiting terms in two distinct but related ways: (a) by allowing the selection of coronagraph architectures with relaxed inner working angles (IWAs), and (b) by pushing the DH out to a focal-plane region that corresponds to higher spatial frequencies in the pupil-plane.

First, because coronagraph sensitivity to low-order aberrations tends to trade with IWA, this suggests that—for a fixed on-sky IWA—a UV coronagraph instrument can be designed with better passive insensitivity to static and dynamic low- to mid-order aberrations compared to a visible-wavelength instrument. For example, a charge-10 VVC at 300 nm has approximately the same IWA as a charge-4 VVC at 600 nm[33], but higher tolerance (in an absolute sense) to low-order aberrations, which implies that a carefully-designed UV coronagraph could actually have relaxed tolerances on observatory performance compared to its visible counterpart.

The second moderating influence can be understood by considering the wavelength-dependence of the contrast at a fixed angular separation. The contrast contribution from Talbot-propagated surface errors (to the first order), scattering, and beam walk at a fixed on-sky angular separation all have an identical wavelength dependence given by

$$C \propto \left(\frac{\alpha_n}{\alpha_{n,0}}\right)^2 \left(\frac{\lambda_0}{\lambda}\right)^4, \tag{7}$$

where α_n is the RMS surface error at spatial frequency n (cycles/aperture) and $\alpha_{n,0}$ is the RMS at spatial frequency $n_0 = n\lambda/\lambda_0$. If optical surface errors are assumed to follow a simple power-law PSD of the form $(n/D)^{-c}$, then (plugging this PSD into Equation 7) the contrast degradation with wavelength scales as

$$C \propto \left(\frac{\lambda_0}{\lambda}\right)^{4-c}. \tag{8}$$

For high-quality optics, $c \approx 2.5$, so the contrast would be expected to scale as $\lambda^{-1.5}$. A power law, however, is a poor approximation of the PSD in the spatial frequency region that corresponds to typical dark hole separations. A better approximation of fabricated optics typically used in high contrast imaging applications is given by[17, 27]

$$\mathrm{PSD}(n) = \frac{a}{1 + (n/b)^c}, \tag{9}$$

where b is the knee frequency (in units of cycles per aperture) and a sets the peak power of the PSD (often ignored in favor of RMS normalization). The knee frequency is typically ∼3 cycles/aperture[17]. Plugging this PSD into Equation 7, the contrast scales in a less straightforward way, with a form given by

$$C \propto \frac{\left(\frac{\lambda_0}{\lambda}\right)^c + \left(\frac{n}{b}\right)^c}{1 + \left(\frac{n}{b}\right)^c} \left(\frac{\lambda_0}{\lambda}\right)^{4-c} \tag{10}$$

The scaling has a strong dependence on the location of the PSD knee b relative to the DH separation angles, but by looking at the limits of this expression, we can write down a rule-of-thumb for the contrast scaling:

$$C_{\mathrm{IWA}} \propto \left(\frac{\lambda_0}{\lambda}\right)^4 \tag{11}$$

$$C_{\mathrm{OWA}} \propto \left(\frac{\lambda_0}{\lambda}\right)^{4-c} \tag{12}$$

In other words, the contrast scales with wavelength as a power law with an exponent between -4 and $c-4$, depending on the separation angle under consideration. In reality, this approximation for C_{IWA} is likely somewhat pessimistic, and C_{OWA} is somewhat optimistic.

The contrast scaling due to quantization and noise on the DM electronics are also moderated by considering a fixed angular separation. Both of these terms scale according to

$$C \propto \left(\frac{\lambda_0}{\lambda}\right)^2 \exp\left\{-\left[\frac{n}{n_{\mathrm{infl}}}\right]^2\left[1-\left(\frac{\lambda}{\lambda_0}\right)^2\right]\right\}, \tag{13}$$

where $n_{\mathrm{infl}} = \frac{\sqrt{2}n_{\mathrm{act}}}{2\pi\omega\Gamma}$ and Γ is the Lyot stop fraction. Assuming typical values for a coronagraph system with a Kilo-C DM[28], the quantization-limited contrast at $6\lambda/D$ at $\lambda = 200\,\mathrm{nm}$ is a factor of $\sim$6 larger compared to $\lambda_0 = 600\,\mathrm{nm}$ at the same separation ($2\lambda_0/D$). At $14\lambda/D$, this factor reduces to $\sim$0.8.

4 Milestone Definitions and Success Criteria

Table 2 summarizes the three major milestones of this project. Milestones 1 and 3 are focused on the development of models and budgets for UV coronagraphy, and Milestones 2a and 2b are focused on experimental validation of these models and demonstrations of high contrast imaging in a testbed environment.

Milestone 1: Completion of a testbed contrast budget at central wavelengths from 200 to 400nm, in bandwidths up to 20%

The contrast budget will break down UV contrast performance limits into the individual components that contribute to the overall contrast performance, informed by metrology of as-built components. In particular, the budget will report the spectral/chromatic performance of each term in the budget as a function of central wavelength and as a function of bandwidth. It will also identify the wavelength/bandwidth regimes in which particular terms dominate the budget and how this is influenced by the two coronagraph architectures considered.

Success criterion: The UV contrast budget will be validated by extending predictions to the visible-wavelength regime and showing that the predicted contrast agrees with the measured testbed performance to within a factor of 2.

Milestone 2: Laboratory demonstration of coronagraphy at UV in vacuum

The goal of this milestone is the validation of the testbed contrast budget from Milestone 1a with a demonstration of high contrast imaging in a vacuum environment. The performance

#	Year	Milestone name
1	1	Completion of a testbed contrast budget at central wavelengths from 200 to 400nm, in bandwidths up to 20%
2a	3	Laboratory demonstration of SPC performance at UV wavelengths in vacuum and validation of testbed contrast budget
2b	3	Laboratory demonstration of VVC performance at UV wavelengths in vacuum and validation of testbed contrast budget
3	3	Completion of a notional HWO contrast budget that closes at 10^{-10} contrast at central wavelengths from 200 to 400nm, in bandwidths up to 20%

Table 2: *Project milestones*

will be quantified by measuring the contrast in a half-sided dark hole, both as a mean over the dark hole and as a function of radial separation. Contrast measurements will be made with both coronagraph masks (SPC and VVC), and as a function of central wavelength and bandwidth. A paper will be published reporting the performance of the testbed and the extent to which the developed contrast budget accurately predicted testbed performance and in-situ Mueller matrix measurements matched polarization modeling.

Milestone 2a: Laboratory demonstration of SPC performance at UV wavelengths in vacuum and validation of testbed contrast budget

Success criterion: Measurement of testbed contrast (defined in Section 6.1) in the SPC layout (Figure 2(a)) at ≥ 3 *central wavelength in the 200-400 nm range and in configurations with a narrowline laser source (*$\ll 1\%BW$*) and broadband source with* $\geq 5\%$ *and* $\leq 20\%$ *BW. The SPC contrast will be measured over a* $\sim 6-14\lambda/D$ *DH. No specific contrast goal is specified here; instead, the criterion is agreement with the predictions from the contrast budget and testbed performance modeling (from Milestone #1) to within a factor of 2.*

Milestone 2b: Laboratory demonstration of VVC performance at UV wavelengths in vacuum and validation of testbed contrast budget

Success criterion: Measurement of testbed contrast (defined in Section 6.1) in the VVC layout (Figure 2(b)) at a central wavelength in the 200-400 nm range and in configurations with a narrowline laser source ($\ll 1\%BW$*) and broadband source with* $\geq 5\%$ *and* $\leq 20\%$ *BW. The exact central wavelength and largest bandwidth will be driven by the specifications of the fabricated VVC unit. The VVC contrast will be measured over a* $\sim 3-10\lambda/D$ *DH. No specific contrast goal is specified here; instead, the criterion is agreement with the predictions from the contrast budget and testbed performance modeling (from Milestone #1) to within a factor of 2.*

Milestone 3: Modeling and contrast budget for an HWO-like UV coronagraph instrument that closes at 10^{-10} contrast. This budget and simulation effort will incorporate inputs from an HWO engineering architecture concept (EAC) observatory model (including a segmented aperture) and feed into a notional UV coronagraph design, taking component metrology and lessons-learned from testbed demonstrations into account. Areas where current state-of-the-art is not sufficient for UV coronagraphy at the 10^{-10} contrast level will be identified. Finally, based on the outcomes of the contrast budget, we will explore the trades

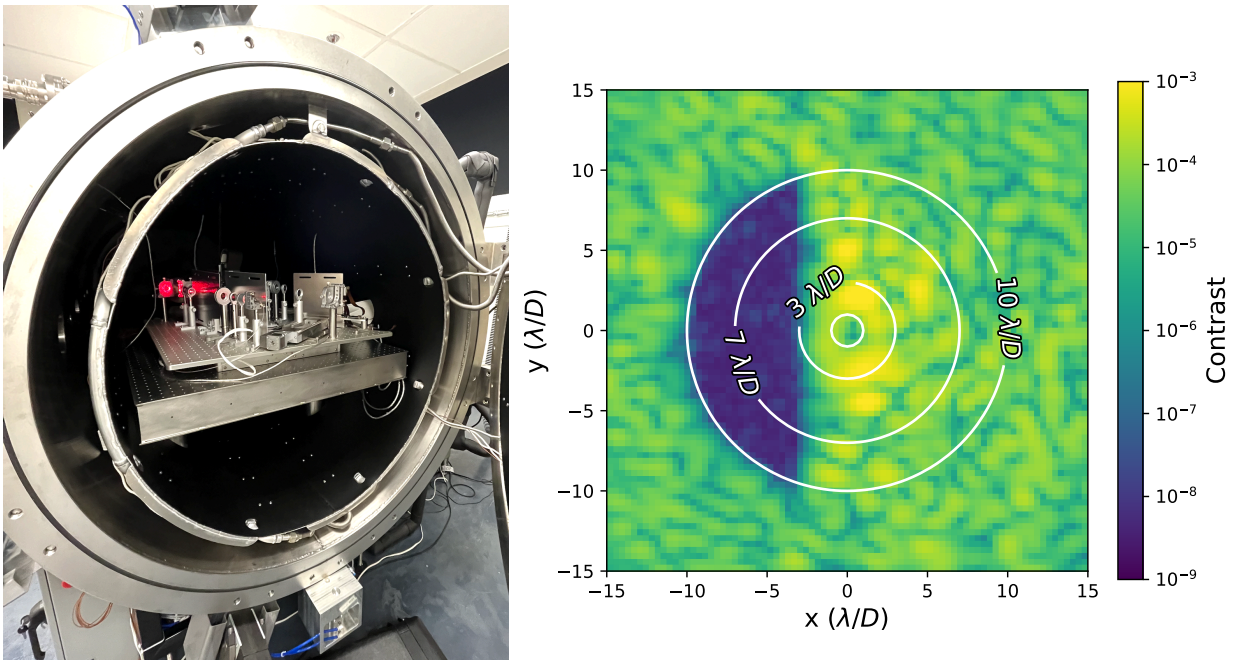

Figure 1: *Left: SCoOB testbed in the UArizona TVAC chamber. Right: Half-sided DH from 3-10λ/D at 633nm with a vector vortex coronagraph dug via iEFC on SCoOB.*

that can be made to achieve 10^{-10} contrast in the UV and provide recommendations for designs to minimize problematic terms.

Success criterion: End-to-end contrast simulations for a HWO-like observatory and UV coronagraph instrument and a budget that achieves 10^{-10} contrast at a central wavelength from 200-400nm and 5% $\leq$ BW $\leq$ 20%.

5 Experiment Description

5.1 Testbed description

The Space Coronagraph Optical Bench (SCoOB) is a prototype vacuum-compatible coronagraph testbed under development at UoA under the direction of Co-I Ewan Douglas. The prototype will serve as a laboratory facility that enables UoA to develop high-contrast imaging technology in support of spaceborne coronagraphic instruments. In its current configuration, the testbed features a 952-actuator Kilo-C continuous-facesheet DM from Boston Micromachines Corp., a VVC manufactured by Beam Co., and a low read-noise, vacuum-compatible CMOS sensor. The off-axis parabolas (OAPs) are protected aluminum (Al+MgF2) with high throughput down to 200 nm and low roughness ($\lesssim$ 0.5 nm RMS surface error on spatial scales smaller than 0.08mm). A multi-layered mechanical isolation system including pneumatic legs through the chamber and a Minus K platform maintains jitter $\lesssim 0.002\lambda/D$ RMS at vacuum. It was recently expanded to accommodate a field stop for additional scattered light mitigation. The system has achieved $\sim 2 \times 10^{-9}$ contrast under

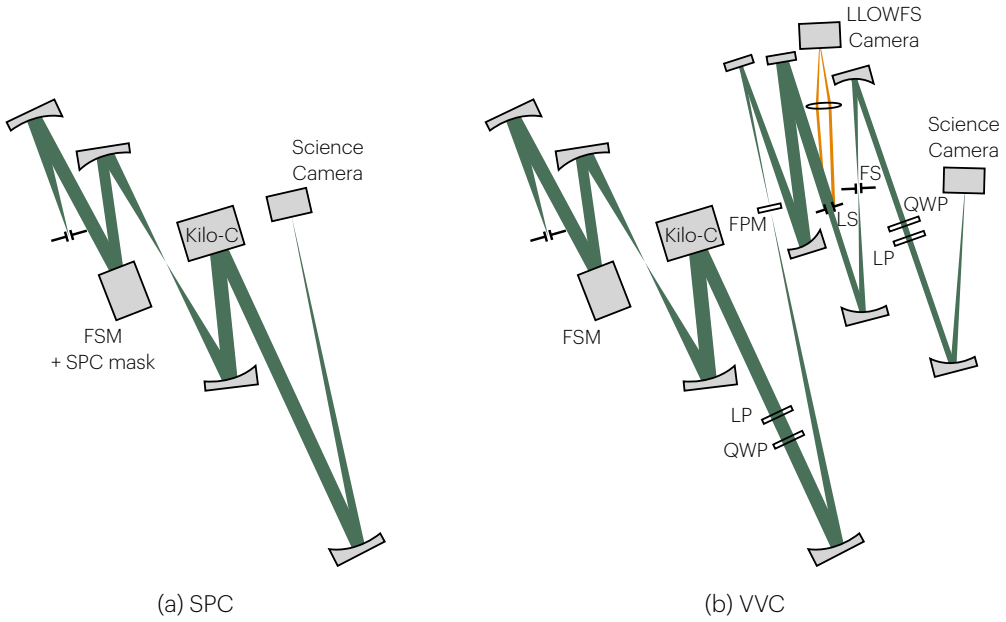

Figure 2: *Optical layouts of the SCoOB testbed for the two coronagraph configurations: (a) SPC and (b) VVC. Reproduced from Van Gorkom et al. 2025[23].*

vacuum at $\sim 3 \times 10^{-6}$ Torr[56].

The DM controller is the commercial off the shelf (COTS) controller supplied by BMC, supplemented with a low-noise pseudo 16-bit filter board capable of a minimum actuator step size of 20 pm. Quantization error at this level is expected to limit the achievable contrast to $\lesssim 5 \times 10^{-10}$ at 350nm and $\lesssim 10^{-9}$ at 250nm [28]. The DM coating is unprotected aluminum with reflectance >80% down to 250 nm. DM surface errors (including print-through and other features resulting from microfabrication) present on MEMS devices are expected to become problematic at UV wavelengths. Preliminary simulations incorporating measured MEMS surfaces suggest this effect is not the limiting contrast factor on SCoOB, but further measurements and modeling are required to account for surface features at high spatial frequencies.

To approximate an unresolved point source, the SCoOB team fabricated a 4µm-diameter high precision pinhole (30% λ/D at 630nm)[57]. As part of this effort, a high-quality 2µm was also fabricated and can be easily swapped into the testbed in case partial resolution of the current pinhole becomes a limiting factor at shorter wavelengths.

For this project, two configurations of the testbed are required for the SPC and VVC masks, shown in Figure 2. The VVC layout is essentially identical to the current layout of SCoOB, with the focal plane maks (FPM), polarization filters, and cameras swapped out for their UV counterparts. The SPC layout makes use of a subset of the optical train, with the SPC mask co-located with the fast steering mirror (FSM) and a single relay to the DM in a conjugate pupil. The science camera is placed in the f/48 focal plane downstream of the DM. Apart from this, a handful of small modifications will be made to the testbed to

support experiments in the UV:

1. UV source: Initial contrast experiments on the testbed will make use of narrowband, frequency-stabilized laser sources at wavelengths in the 200-400 nm regime. Once narrowband performance is understood, a supercontinuum source and wavelength tuner with UV coverage will be swapped in.

2. UV-sensitive detector: The current science camera on the SCoOB testbed is a Sony IMX571 CMOS chip with $\sim 1e^-$ read noise and a 16-bit ADC, packaged in a vacuum-compatible housing developed by Neutralino Space Ventures. To increase the effective quantum efficiency (QE) in the UV, the baseline plan is to apply a fluorescent coating to the CMOS chip to down-convert the incident UV wavelengths to the visible, where the unmodified sensor QE is high. The application of the coating has been shown to not degrade the sensor performance [58]. The current science camera is highly oversampled at 630nm and maintains better-than-Nyquist sampling down to 250nm. As an alternative, the Sony IMX487 is a CMOS sensor that offers QE >20% as short as 200nm and is available from a number of commercial vendors. We already have one such sensor (controlled by Co-I Ewan Douglas), and it can be re-packaged in-house for vacuum compatibility.

3. UV coronagraph masks: A UV VVC will be procured from Beam Co. Our team has worked with Beam Co. to fabricate a number of VVC devices for visible wavelengths, and Beam Co. has produced vector vortex waveplates optimized for wavelengths as short as 325 nm. A shaped pupil coronagraph will also be designed and fabricated with Advanced Nanophotonics, who have fabricated high-performing masks for other high contrast testbeds [59]. Carbon nanotubes (CNTs) demonstrate extremely low reflectivity at UV wavelengths, making them an optimal choice for extending reflective SPC technology into the UV [60]. In addition, as collaborators on an SAT to demonstrate black silicon (BSi) masks for high contrast imaging (PI A.J. Riggs), we will also receive BSi SPC masks and explore the performance of these masks at UV wavelengths.

5.2 Performance predictions and models

Initial modeling of the SCoOB testbed at UV wavelengths with an end-to-end Fresnel model built in HCIPy[61] and scattering from surface roughness has already been performed[23]. This contrast budget includes chromatic residuals from surface and reflectivity errors, fabrication errors on the coronagraph masks, scattering, jitter and beam walk, polarization aberrations, DM quantization, and actuator noise. HCIPy natively supports the simulation of polarized electric fields, so we also directly incorporate polarization optics (including retardance errors and finite extinction) in the Fresnel simulations. An incoherent floor due to scattering from surface roughness not captured in the diffraction model is separately computed following the approach adopted for PICTURE-C performance modeling[27]. We reproduce the table summarizing the contrast budgets for the SPC and VVC configurations in Tables 3 and 4.

We perform the polarization modeling using polarization ray tracing to estimate the Jones pupils (amplitude and phase maps) at intermediate planes in the optical train and integrate it with the Fresnel model. Independently, we will estimate the Jones pupil at the exit pupil for both the configurations (after Kilo-C DM in Fig. 2a and after LP in Fig. 2b). These Jones pupils are converted to intensity-based 4×4 Mueller matrix that can be measured

using a dual rotating polarization generator (at the source) and analyzer (at the exit pupil) for verification between the simulation and measurement.

These performance predictions do not account for a number of sources that may limit contrast—including scattering from particulate contamination and ghosts from back-reflections—and rely on extrapolation from current metrology (e.g., surface roughness measurements of as-built optics do not capture errors beyond some spatial frequency). Updating the performance predictions based on component metrology and refining the integrated model is a significant part of this effort.

Term	200 nm	300 nm	400 nm
Chromatic EFC residuals (surface and reflectivity errors)	2%: 3.4×10^{-9} 5%: 1.6×10^{-8} 10%: 5.6×10^{-8}	2%: 2.1×10^{-9} 5%: 8.9×10^{-9} 10%: 3.3×10^{-8}	2%: 2.1×10^{-9} 5%: 8.4×10^{-9} 10%: 3.4×10^{-8}
Mask specular reflectivity	2.0×10^{-10}	1.4×10^{-10}	1.4×10^{-10}
Mask diffuse reflectivity	4.4×10^{-11}	1.5×10^{-10}	3.3×10^{-10}
Mask fabrication errors	2%: 9.7×10^{-11} 5%: 1.8×10^{-10} 10%: 5.9×10^{-10}	2%: 1.6×10^{-10} 5%: 2.3×10^{-10} 10%: 5.6×10^{-10}	2%: 2.2×10^{-10} 5%: 3.0×10^{-10} 10%: 5.2×10^{-10}
Scattering (surface roughness)	1.4×10^{-11}	1.4×10^{-11}	1.4×10^{-11}
Jitter and beamwalk	4.4×10^{-11}	1.6×10^{-11}	8.5×10^{-12}
Polarization aberrations	1.6×10^{-10}	2.6×10^{-10}	8.2×10^{-10}
DM quantization	4.0×10^{-11}	1.8×10^{-11}	1.0×10^{-11}
DM noise	7.8×10^{-11}	3.5×10^{-11}	2.0×10^{-11}
Total contrast	2%: 4.1×10^{-9} 5%: 1.7×10^{-8} 10%: 5.8×10^{-8}	2%: 2.9×10^{-9} 5%: 9.8×10^{-9} 10%: 3.4×10^{-8}	2%: 3.4×10^{-9} 5%: 9.8×10^{-9} 10%: 3.6×10^{-8}

Table 3: *Contrast budget for the SPC layout for central wavelengths λ_0 from* 200-400 nm*, and bandwidths from 2-10%. The dark hole is a D-shaped, half-sided DH from $6 - 14\lambda_0/D$. The individual terms are incoherently added to produce the total contrast floor. Reproduced from Van Gorkom et al. 2025[23].*

5.3 Experiment plans

This project adopts a multi-pronged approach to advance the state-of-the-art in UV high contrast imaging, combining detailed modeling (both analytic and numerical) of physical optics to produce a contrast budget, component-level metrology, and validation of the contrast budget through a testbed demonstration. To aid in disentangling architecture- and wavelength-specific effects, the project will simultaneously explore two complementary coronagraph designs: a vector vortex coronagraph (VVC)[2–6] and a shaped pupil coronagraph (SPC)[7–9]. As a final product, the team will leverage the validated contrast budget to produce predictions of science yield informed by contrast performance and UV coverage.

Term	200 nm	300 nm	400 nm
Chromatic EFC residuals (surface and reflectivity errors)	2%: 4.7×10^{-9} 5%: 2.3×10^{-8} 10%: 7.9×10^{-8}	2%: 1.5×10^{-9} 5%: 7.7×10^{-9} 10%: 2.7×10^{-8}	2%: 9.2×10^{-10} 5%: 4.0×10^{-9} 10%: 1.4×10^{-8}
Stop specular reflectivity	2.0×10^{-11}	8.9×10^{-12}	7.9×10^{-12}
Stop diffuse reflectivity	3.0×10^{-11}	8.0×10^{-11}	1.8×10^{-10}
Scattering (surface roughness)	1.2×10^{-10}	1.2×10^{-10}	1.2×10^{-10}
Jitter and beamwalk	3.6×10^{-9}	4.6×10^{-10}	2.3×10^{-10}
Polarization aberrations	9.0×10^{-13}	5.3×10^{-13}	1.7×10^{-12}
Polarization leakage	6.9×10^{-11}	6.3×10^{-11}	6.2×10^{-11}
DM quantization	8.2×10^{-11}	3.6×10^{-11}	2.1×10^{-11}
DM noise	1.6×10^{-10}	7.1×10^{-11}	4.0×10^{-11}
Total contrast	2%: 9.0×10^{-9} 5%: 2.7×10^{-8} 10%: 8.3×10^{-8}	2%: 2.3×10^{-9} 5%: 8.5×10^{-9} 10%: 2.8×10^{-8}	2%: 1.9×10^{-9} 5%: 5.0×10^{-9} 10%: 1.5×10^{-8}

Table 4: *Contrast budget for the VVC layout for central wavelengths λ_0 from* 200-400 nm*, and bandwidths from 2-10%. The dark hole is a D-shaped, half-sided DH from $3 - 10\lambda_0/D$. The individual terms are incoherently added to produce the total contrast floor. Reproduced from Van Gorkom et al. 2025[23].*

5.3.1 Contrast budget

As the first step toward UV coronagraphy, we propose to produce a thorough contrast budget—which separates out the individual terms that contribute to the total achievable contrast—in order to understand which terms ultimately limit the performance of the coronagraph system. A contrast budget also enables investigations into the chromatic performance of the system and the wavelength regimes in which different terms dominate the contrast budget. This analysis will be performed by building analytic models and scaling laws where possible and cross-checking with numerical simulations of these terms. Although the individual terms in the budget can be considered independently, an integrated budget must take into account the instrument or telescope as a whole in order to produce performance predictions. We will develop a UV contrast budget for two systems: one for the SCoOB testbed with an SPC and VVC coronagraph and one that closes at the 10^{-10} contrast for comparison to HWO needs. The former enables validation of the budget (and the analytical tools that produce it) with the proposed effort in component metrology and contrast experiments in the vacuum testbed, while the latter enables us to explore instrument requirements for HWO coronagraphy at UV wavelengths and make performance and yield predictions.

The contrast budget will be analyzed for a range of central wavelengths as short as 200 nm, and a range of bandwidths up to 20%. A number of the terms expected to be most significant at the UV have already been identified—including surface aberrations and roughness (including DM print-through), polarization aberrations, coating non-uniformities, and mask fabrication errors—but their behavior at UV wavelengths has not be carefully or systematically studied.

We will partially guide laboratory efforts to improve UV coronagraph performance with models of ozone detectability in Earth-like exoplanetary atmospheres. Using a suite of existing model-derived Earth-like atmospheres at different oxygenation levels [62] and an open-source reflected-light retrieval model [63], we will search for thresholds where ozone detection could dramatically improve or degrade. Here, inverse studies with varied shortwave UV cutoffs as well as varied spectrally-dependent contrast (informed by early laboratory results) will reveal where additional breakthroughs in spectral coverage and/or delivered contrast would strongly increase future science performance in terms of ozone detectability.

5.3.2 Component metrology

To aid in isolating individual error terms in the contrast budget and updating it with as-built values that can inform performance predictions, we propose a significant effort in component-level metrology. This work serves multiple purposes: it updates the testbed contrast budget with realistic values, serves as a cross-check of assumptions in a general budget (e.g., answering questions like whether the surface roughness of the optics follows the assumed statistics), and could identify areas where current state-of-the-art fabrication techniques fall short of the requirements for UV coronagraphy.

High-resolution surface metrology will provide measurements key to constraining and updating the power spectral densities (PSDs) assumed in the surface roughness models in the contrast budget and simulations. A single metrology device can typically measure only a subset of the spatial frequencies of interest, but by combining measurements from multiple devices we can constrain the PSD over a broad range of frequencies. A 4D PhaseCam 6000 (controlled by Co-I Ewan Douglas), capable of sub-nanometer surface measurements on 10s of µm lateral scales (dependent on the configuration), will provide information on low- to mid-spatial frequency content. The Zygo NewView 8300, a coherence-scanning white light interferometer with a lateral resolution of 0.34µm and a surface height precision of 0.2nm ($\lambda/1000$ at 200nm), will provide measurements of surface roughness and the quality of the shaped pupil mask fabrication. With the scanning functionality of the NewView 8300, we can also make high-resolution measurements of the DM print-through pattern and microfabrication features.

To fully capture scattering behavior out to the maximum scattering angles, knowledge of surface roughness to the single-wavelength spatial resolution is required [27]. To complete the measurements of surface roughness to sub-wavelength spatial scales, we will use a non-contact atomic force microscope (AFM)—the Park NX20—with nanometer-scale lateral resolution and sub-angstrom height precision. Measurements will be made of a sample of representative off-axis parabolas (OAPs), SPC mask, flat mirrors, and the MEMS DM.

To validate the model that predicts scatter from surface roughness directly, we also plan to make direct scattering measurements with a Bidirectional Scattering Distribution Function (BSDF) device, the J&C RT300. In spectrometry mode with a broadband Halogen source, the device can measure scattering over a wide range of angles (0-60°) as a function of wavelength (from NUV to visible). These measurements will be compared to the scattering predictions generated from the roughness data collected above.

Spatial and spectral variations in the retardance, transmission, and fast axis of the vector vortex waveplate can cause leakage into the orthogonal polarization state that results in

localized incoherent and chromatic speckle features in the focal plane. These features have been previously noted at visible wavelengths [64], but they have not been modeled in high-fidelity simulations, and the scale of their effect on contrast in the UV is unknown. To update the polarization component of the contrast budget, we propose to measure the VVC and polarization optics with a Mueller matrix spectropolarimeter, a device that yields a spatial map of all components of the Mueller matrix as a function of wavelength. Integrating spatial Mueller matrix data into coronagraph simulations enables predictions of contrast limitations due to mask features and helps disentangle contrast limits due to instrument effects from mask defects. The Deep-UV variant of the Axostep Mueller Matrix Imaging Polarimeter can measure the Mueller matrix with $\sim 2\mu$m lateral resolution down to a wavelength of 200nm. This device can also be operated in reflection, enabling measurements of the spatial variation of polarization properties (due to non-uniformities in the thickness of coating layers, which leads to amplitude and phase variations in the orthogonal polarization states) across the surface of the OAPs and other reflective optics. All these measurements will be integrated into an updated contrast budget to generate an as-built performance prediction for SCoOB UV operations.

5.3.3 Testbed validation

The third major component of the project is to validate the developed contrast budget with a demonstration of UV high contrast imaging on SCoOB. To enable differentiation of architecture-specific limitations from other elements in the contrast budget, we propose two major tasks on the SCoOB testbed. The first is a direct measurement of the testbed Mueller matrix at UV wavelengths, and the second is a set of contrast experiments with UV-optimized coronagraph masks.

An initial effort to directly measure the end-to-end Mueller matrix of the testbed exit pupil at visible wavelengths made use of an in-situ dual-rotating-retarder Mueller polarimeter to quantify how polarization aberrations couple in speckle residuals[65]. We propose to extend this work into the UV to provide a direct comparison to and validation of the simulations that predict polarization aberrations at UV wavelengths as a function of the optical design of the instrument.

For the second task, two coronagraph masks—the UV-optimized VVC and SPC—will be integrated into the testbed, and a series of contrast experiments in vacuum and air will be performed over a range of UV wavelengths and bandpasses to establish the highest possible contrast performance.

The SPC creates a dark zone—the region of high contrast in the focal plane—via a binary amplitude mask in the pupil plane. (By binary, we mean that a point in the mask is either fully obscured or fully unobscured.) This is the one of simplest coronagraphs, and it requires few optics, thereby reducing the throughput penalty due to low reflectance in the UV and contrast degradation due to scattering and surface errors on out-of-pupil optics. It is also inherently achromatic and relatively robust to polarization, wavefront aberrations, misalignments, and the presence of dust. An SPC design that theoretically produces better than 1×10^{-10} contrast in the UV for the segmented HWO pupil will appear as a point design in an upcoming white paper by the Coronagraph Design Survey UV-Vis working group. We propose to fabricate an SPC mask for an unobscured circular aperture to create a radial

dark zone from 6-14 λ/D.

The VVC comprises a spatially-varying halfwave plate in a focal plane with a Lyot stop in a downstream pupil plane. The optical axis of the halfwave plate varies azimuthally to accumulate an integer-multiple number of 2π radians of phase in one complete rotation, the result of which is that the light from on-axis source is remapped to outside the geometrical pupil in a downstream pupil plane. This integer multiple is referred to as the charge of the device. VVCs have been shown to be capable of producing high contrast and high throughput in the laboratory environment, including the Decadal Survey Testbed (DST)[66], the High Contrast Spectroscopy Testbed for Segmented Telescopes (HCST)[67], the High Contrast Imaging Testbed (HCIT)[68–70], as well as ground-testing for the PICTURE-C mission[71]. The DST recently achieved 1.57×10^{-9} contrast in a 10% bandpass and 5.86×10^{-9} in a 20% bandpass[64]. The SCoOB testbed currently has a charge-6 VVC with a 20% bandpass centered around 630nm. To facilitate the UV effort, we propose to have a similar VVC fabricated, optimized to a central wavelength in the 250-350nm range.

6 Data Measurement & Analysis

The two primary types of data acquired as part of this project are testbed measurements of contrast and (b) component-level metrology. The definitions and approach to analysis of testbed measurements here largely follows those adopted in the milestone white paper of Serabyn et al. 2019.

6.1 Definitions

The simulated "star" is a small (2-4µm diameter) pinhole illuminated with light relayed from a fiber source at the front-end of the optical system. The pinhole is unresolved by the optical system.

The "raw" images are arrays of pixel-by-pixel counts directly from the sensor. "Calibrated" images are raw images after subtraction of a background image (a raw image taken with the source blocked and with the camera in the same configuration) and conversion into counts/sec by normalization by the sensor integration time. Calibrated images could also include a normalization to account for detector gain and a known attenuation of the source, but we generally avoid these additional steps to reduce the influence of calibration errors. Measurements of normalized intensity (NI) are performed on calibrated images.

The "dark zone" (or dark hole) is the focal plane region (the extent of which is typically measured in units of λ/D) targeted by the combination of coronagraph mask and the dark-hole digging algorithm for a minimum residual intensity from the on-axis stellar source.

The NI is a measure of the contrast, computed as the ratio of detector pixel counts to the peak counts of the stellar PSF under the same testbed configuration (source brightness, bandwidth, etc.).

The mean NI is the unweighted average of the NI over the dark zone pixels, where the dark zone extent is defined based on the central wavelength of the bandpass.

To ensure that the contrast is reported with high statistical confidence, we assume Gaussian statistics on the noise on estimates of the NI computed from independent detector

frames. From a set of N images, the mean contrast is calculated as

$$\hat{c} = \frac{1}{N}\sum_{n=1}^{N} c_n, \tag{14}$$

where c_n is the NI calculated for a single frame. The variance on this contrast estimate is given by

$$\sigma^2_{\text{meas}} = \frac{1}{N-1}\sum_{n=1}^{N}(c_n - \hat{c})^2 \tag{15}$$

with uncertainty

$$\sigma_{\text{mean}} = \frac{\sigma_{\text{meas}}}{\sqrt{N}} \tag{16}$$

The statistical confidence that an estimated contrast value is less than some value c_0 is given by

$$\text{conf} = \frac{1}{\sqrt{2\pi}}\int_{\infty}^{t} e^{-z^2/2}dz, \tag{17}$$

where $t = (c_0 - \hat{c})/\sigma$, $\sigma^2 = \sigma^2_{\text{mean}} + \sigma^2_{\text{phot}}$, and σ^2_{phot} is the variance on the photometric reference. We assume a required confidence of 90% for milestones tied to contrast performance.

6.2 Measurement of polarization aberrations

Polarization aberrations will be measured as a 4×4 Mueller matrix ($\mathbf{M}$) at the testbed exit pupil. The measured Mueller matrix can be decomposed into a product of three individual Mueller matrices following the Lu-Chipman [72] decomposition that describes the polarization aberrations of the system, where $\mathbf{M}_\Delta$ is the depolarizer, $\mathbf{M}_r$ is the retarder, and $\mathbf{M}_d$ is the diattenuator:

$$\mathbf{M} = \mathbf{M}_\Delta \mathbf{M}_r \mathbf{M}_d. \tag{18}$$

We will estimate diattenuation (d) as

$$d = \frac{\sqrt{M_{01}^2 + M_{02}^2 + M_{03}^2}}{M_{00}}, \tag{19}$$

and retardance (δ) as

$$\delta = cos^{-1}\left(\frac{Tr(\mathbf{M})}{2} - 1\right)., \tag{20}$$

and the depolarization index (DI) as

$$DI(\mathbf{M}) = \frac{\sqrt{(\sum_{i,j} M_{i,j}^2) - M_{00}^2}}{\sqrt{3}M_{00}}. \tag{21}$$

Each of these quantities varies spatially across the exit pupil. To quantify the agreement between the measured and modeled values, we will compute the root mean square (RMS) of the difference maps

$$\mathrm{RMS}(x) = \sqrt{\frac{1}{N_p}\sum_{n=1}^{N_p}\left[x(n) - \hat{x}(n)\right]^2}, \tag{22}$$

where $x(n)$ is the measured value of the quantity at pixel n, $\hat{x}(n)$ is its modeled value, and N_p is the total number of pixels over the pupil.

Diattenuation d and depolarization index DI are intrinsically normalized to unity, so the RMS can be immediately interpreted as a fractional error. The retardance δ is given in radians in Equation 20 but can be converted to a fractional wave for comparison to the modeled values:

$$\delta_\lambda = \frac{\delta}{2\pi} \tag{23}$$

6.3 Measurement of star brightness

The procedure for measuring the star brightness depends on the coronagraph mask installed in the testbed. To account for drift in the source power and coupling to the pinhole, this step is performed at the beginning of any contrast experiment (after allowing the source to settle) and at the end of the experiment as a consistency check. In the case of the VVC, the procedure is:

1. Drive the PSF off-axis by $\geq 20\lambda/D$ from the center of the FPM.
2. Take calibrated measurements of the non-saturated core of the PSF. Saturation can be avoided by adjusting camera integration times and/or attenuating the source brightness by a known amount.
3. Estimate the peak counts by either directly measuring the peak pixel (counts/sec) or fitting a model of the PSF to the measured data.

In the case of the SPC, the PSF is approximately shift-invariant and does not need to be driven off-axis. The procedure is identical to the above, with the exception that step #1 can be skipped.

6.4 Measurement of coronagraph dark hole contrast

With the PSF aligned to the FPM (in the case of the VVC) and typically after performing wavefront sensing and control, the coronagraph dark hole contrast is measured by taking a long exposure (typically tens of milliseconds to seconds) of a camera subarray that covers the dark zone of interest. The contrast as NI (defined above) is estimated by computing the calibrated image and normalizing by the peak star counts.

As SCoOB features only a single DM, dark zones will be a half-sided, D-shaped region. In the case of the VVC, the nominal dark zone spans $3 - 10\lambda_0/D$, where λ_0 is the central wavelength of the source bandpass. With the current design of the SPC mask, the nominal dark zone spans $6 - 14\lambda_0/D$.

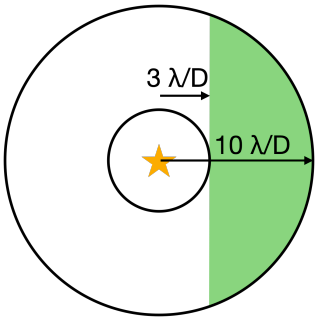

Figure 3: *The dark hole region targeted in the VVC configuration, spanning a D-shaped half-sided focal plane region from* $3-10\lambda_0/D$. *The region targeted in the SPC configuration has the same geometry but an inner edge at* $6\lambda_0/D$ *and an outer edge at* $14\lambda_0/D$.

6.5 Milestone demonstration procedure

Experiment trials tied to milestones will be repeated three times to demonstrate repeatability of the result. For demonstrations of contrast on the testbed (Milestones 3a and 3b), the procedure for a single trial will be:

1. From a system "off" state, power on the DM, laser source, and any other powered components, and allow the system to settle.
2. Set the DM to a "flat" command. This is a pre-computed command that is determined by phase retrieval at either the science camera or a camera at the FPM position. This command is typically only updated after modifications to the testbed (e.g., install of a new coronagraph mask, re-alignment of any optics, etc.).
3. Take an initial measurement of the star brightness.
4. Perform wavefront sensing and control to optimize the dark zone. This procedure may include one or more calibrations for control algorithms like implicit EFC or LOWFS. Contrast measurements are typically taken at each iteration of the dark hole digging algorithm.
5. Take final measurements of the dark zone contrast after focal-plane wavefront sensing and control, typically a large number of long-exposure images to provide statistical confidence on the contrast estimate. If necessary to maintain the contrast level, LOWFS may be active during these measurements.
6. Repeat the measurement of star brightness to confirm the normalization has not drifted over the measurement.

For validation of the polarization model with testbed polarimetry (Milestone 2), each measurement sequence requires a large number of individual measurements with polarization optics at varying rotations[65]. To demonstrate repeatability, we will reset the polarizer rotations and repeat the measurement sequence a minimum of three times. Additionally, the polarization measurements will take at multiple wavelengths spanning the $200-400\,\mathrm{nm}$ range.

7 Schedule

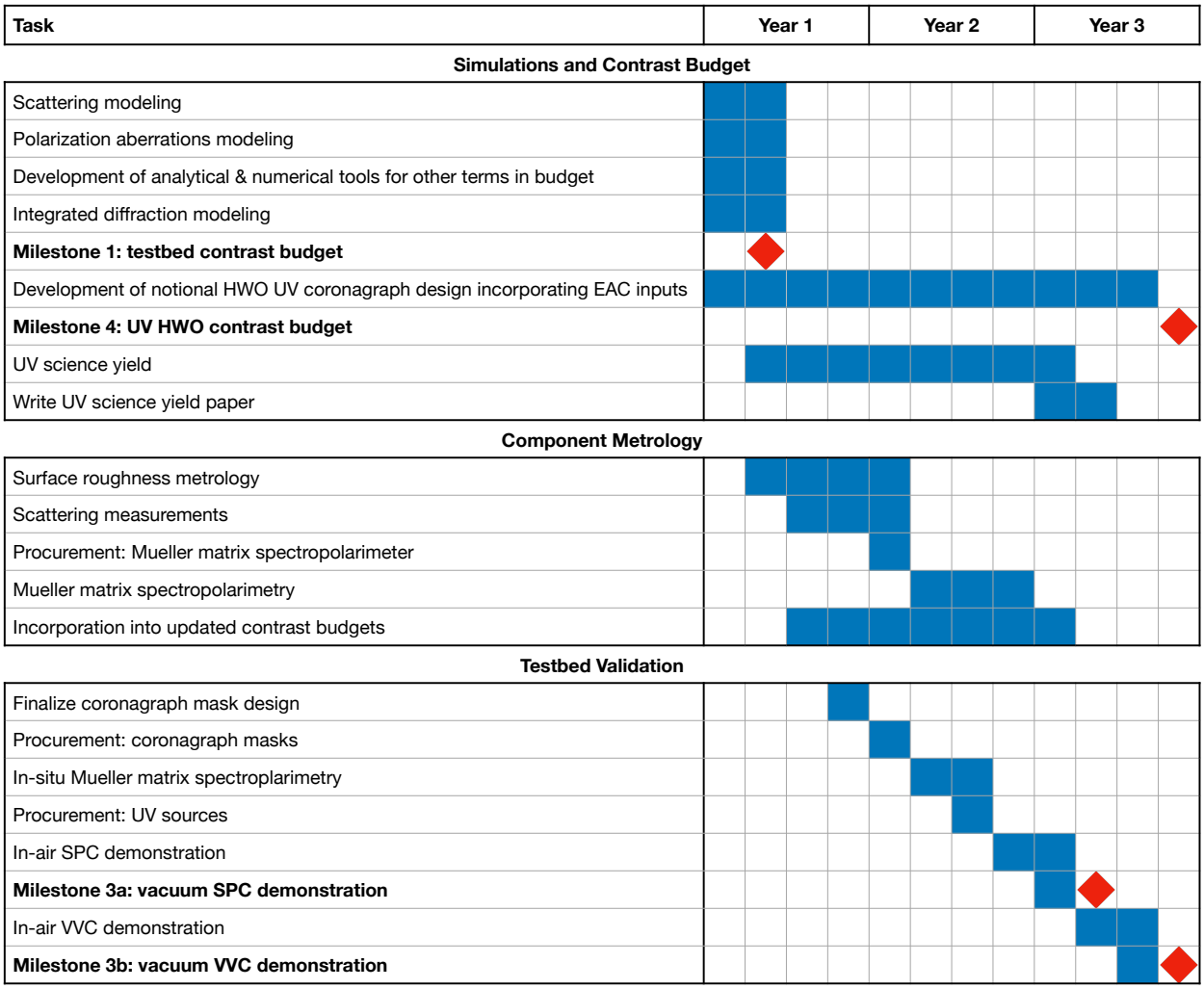

Figure 4: *Work plan for the project*

Year 1: The effort will focus on the development of the UV error budgets and on end-to-end simulations to generate performance predictions and cross-checks of the analytical components of the error budget. This includes the development of a scattering model, the calculation of Jones pupil polarization aberrations from a ray-trace model, and a diffraction model that integrates these effects (as well as the other terms summarized in Table 1). At the same time, the effort to tie instrumental contrast performance to UV science yield will begin and will carry on through the first half of year 3. Milestones 1 is expected to be completed in year one. The design and specification of the SPC and VVC units for SCoOB will also be completed the first year. Component-level metrology will begin in year 1 and continue into year 2. The modeling and contrast budget effort for a HWO UV coronagraph will begin in year 1 and continue through year 3.

Year 2: At the beginning of year two, any remaining long-lead items required for the

testbed validation will be ordered. Component metrology will make up the bulk of the efforts in year two. A sample of representative OAPs, flats, the MEMS DM, and the fabricated SPC will be subjected to surface roughness and scattered light measurements. The VVC, SPC, polarization optics, and OAPs will be measured under a Mueller matrix spectropolarimeter over a range of UV wavelengths. All measured quantities will be compared to the assumptions from the initial contrast budget, and the contrast budgets (and the models from which they are generated) will be updated to incorporate the as-built performance of these components. In-situ Mueller matrix polarimetry will be performed at UV wavelengths.

Year 3: Year three will be focused on validation in the testbed. Since the SPC layout is significantly simpler and the mask itself is achromatic, the SPC will be integrated into the testbed first, and the visible to near-UV performance of the SPC will be evaluated in air. The UV-sensitive detector will be then integrated with the testbed, and in-air UV tests of the SPC will be followed by vacuum tests (Milestone 2a). Afterwards, the SPC will be removed and the VVC will be placed in the FPM plane. In-air tests of the VVC will be performed prior to vacuum tests (Milestone 2b). At the conclusion of the year, a report will be prepared to summarize the outcomes of these experiments. Milestone 3 will be concluded by the end of year 3.

8 References

[1] The LUVOIR Team. "The LUVOIR Mission Concept Study Final Report". In: *arXiv e-prints*, arXiv:1912.06219 (Dec. 2019), arXiv:1912.06219. DOI: 10.48550/arXiv.1912.06219. arXiv: 1912.06219 [astro-ph.IM].

[2] D. Mawet, P. Riaud, O. Absil, and J. Surdej. "Annular Groove Phase Mask Coronagraph". en. In: *The Astrophysical Journal* 633.2 (Nov. 2005). Publisher: IOP Publishing, p. 1191. ISSN: 0004-637X. DOI: 10.1086/462409. URL: https://iopscience.iop.org/article/10.1086/462409/meta (visited on 02/08/2023).

[3] Gregory Foo, David M. Palacios, and Grover A. Swartzlander. "Optical vortex coronagraph". EN. In: *Optics Letters* 30.24 (Dec. 2005). Publisher: Optica Publishing Group, pp. 3308–3310. ISSN: 1539-4794. DOI: 10.1364/OL.30.003308. URL: https://opg.optica.org/ol/abstract.cfm?uri=ol-30-24-3308 (visited on 02/08/2023).

[4] D. Mawet, E. Serabyn, K. Liewer, Ch. Hanot, S. McEldowney, D. Shemo, and N. O'Brien. "Optical Vectorial Vortex Coronagraphs using Liquid Crystal Polymers: theory, manufacturing and laboratory demonstration". en. In: *Optics Express* 17.3 (Feb. 2009), p. 1902. ISSN: 1094-4087. DOI: 10.1364/OE.17.001902. URL: https://opg.optica.org/oe/abstract.cfm?uri=oe-17-3-1902 (visited on 02/08/2023).

[5] Garreth Ruane, Dimitri Mawet, Bertrand Mennesson, Jeffrey B. Jewell, and Stuart B. Shaklan. "Vortex coronagraphs for the Habitable Exoplanet Imaging Mission concept: theoretical performance and telescope requirements". In: *Journal of Astronomical Telescopes, Instruments, and Systems* 4.1 (Mar. 2018). Publisher: SPIE, p. 015004. ISSN: 2329-4124, 2329-4221. DOI: 10.1117/1.JATIS.4.1.015004. URL: https://www.spiedigitallibrary.org/journals/Journal-of-Astronomical-Telescopes-Instruments-and-Systems/volume-4/issue-1/015004/Vortex-coronagraphs-

for-the-Habitable-Exoplanet-Imaging-Mission-concept/10.1117/1.JATIS.4.1.015004.full (visited on 02/08/2023).

[6] Eugene Serabyn, Camilo Mejia Prada, Pin Chen, and Dimitri Mawet. "Vector vortex coronagraphy for exoplanet detection with spatially variant diffractive waveplates". In: *J. Opt. Soc. Am. B* 36.5 (2019), pp. D13–D19. DOI: 10.1364/JOSAB.36.000D13. URL: https://opg.optica.org/josab/abstract.cfm?URI=josab-36-5-D13.

[7] N. Jeremy Kasdin, Robert J. Vanderbei, David N. Spergel, and Michael G. Littman. "Extrasolar Planet Finding via Optimal Apodized-Pupil and Shaped-Pupil Coronagraphs". en. In: *The Astrophysical Journal* 582.2 (Jan. 2003). Publisher: IOP Publishing, p. 1147. ISSN: 0004-637X. DOI: 10.1086/344751. URL: https://iopscience.iop.org/article/10.1086/344751/meta (visited on 01/08/2024).

[8] Robert J. Vanderbei, David N. Spergel, and N. Jeremy Kasdin. "Circularly symmetric apodization via star-shaped masks". In: *The Astrophysical Journal* 599 (2003), pp. 686–694.

[9] Robert J. Vanderbei, David N. Spergel, and N. Jeremy Kasdin. "Spiderweb masks for high-contrast imaging". In: *The Astrophysical Journal* 590 (2003), pp. 593–603.

[10] *2024 Astrophysics Strategic Technology Gaps*. URL: https://apd440.gsfc.nasa.gov/tech_gap-descriptions.html.

[11] *2022 NASA Strategic Plan*. URL: https://www.nasa.gov/ocfo/strategic-plan/.

[12] *Progress in Technology for Exoplanet Missions (Technology Plan Appendix 2023)*. URL: https://exoplanets.nasa.gov/internal_resources/2595/.

[13] Jade H. Checlair, Geronimo L. Villanueva, Benjamin P. C. Hayworth, Stephanie L. Olson, Thaddeus D. Komacek, Tyler D. Robinson, Predrag Popović, Huanzhou Yang, and Dorian S. Abbot. "Probing the Capability of Future Direct-imaging Missions to Spectrally Constrain the Frequency of Earth-like Planets". In: AJ 161.3, 150 (Mar. 2021), p. 150. DOI: 10.3847/1538-3881/abdb36. arXiv: 2101.07378 [astro-ph.EP].

[14] Stephanie L. Olson, Edward W. Schwieterman, Christopher T. Reinhard, Andy Ridgwell, Stephen R. Kane, Victoria S. Meadows, and Timothy W. Lyons. "Atmospheric Seasonality as an Exoplanet Biosignature". In: ApJ 858.2, L14 (May 2018), p. L14. DOI: 10.3847/2041-8213/aac171. arXiv: 1806.04592 [astro-ph.EP].

[15] Zhaohuan Zhu. "Accreting Circumplanetary Disks: Observational Signatures". In: ApJ 799.1, 16 (Jan. 2015), p. 16. DOI: 10.1088/0004-637X/799/1/16. arXiv: 1408.6554 [astro-ph.EP].

[16] Yifan Zhou, Brendan P. Bowler, Kevin R. Wagner, Glenn Schneider, Dániel Apai, Adam L. Kraus, Laird M. Close, Gregory J. Herczeg, and Min Fang. "Hubble Space Telescope UV and Hα Measurements of the Accretion Excess Emission from the Young Giant Planet PDS 70 b". In: AJ 161.5, 244 (May 2021), p. 244. DOI: 10.3847/1538-3881/abeb7a. arXiv: 2104.13934 [astro-ph.EP].

[17] John E. Krist, John B. Steeves, Brandon D. Dube, A.J. Eldorado Riggs, Brian D. Kern, David S. Marx, Eric J. Cady, Hanying Zhou, Ilya Y. Poberezhskiy, Caleb W. Baker, James P. McGuire, Bijan Nemati, Gary M. Kuan, Bertrand Mennesson, John T. Trauger, Navtej S. Saini, and Sergi Hildebrandt Rafels. "End-to-end numerical modeling of the Roman Space Telescope coronagraph". In: *Journal of Astronomical Telescopes, Instruments, and Systems* 9.4 (2023), p. 045002. DOI: 10.1117/1.JATIS.9.4.045002. URL: https://doi.org/10.1117/1.JATIS.9.4.045002.

[18] A. J. Eldorado Riggs, Vanessa Bailey, Dwight C. Moody, Erkin Sidick, Kunjithapatham Balasubramanian, Douglas M. Moore, Daniel W. Wilson, Garreth Ruane, Dan Sirbu, Jessica Gersh-Range, John Trauger, Bertrand Mennesson, Nicholas Siegler, Eduardo Bendek, Tyler D. Groff, Neil T. Zimmerman, John Debes, Scott A. Basinger, and N. Jeremy Kasdin. "Flight mask designs of the Roman Space Telescope coronagraph instrument". In: *Techniques and Instrumentation for Detection of Exoplanets X*. Ed. by Stuart B. Shaklan and Garreth J. Ruane. Vol. 11823. International Society for Optics and Photonics. SPIE, 2021, 118231Y. DOI: 10.1117/12.2598599. URL: https://doi.org/10.1117/12.2598599.

[19] Johan Mazoyer and Laurent Pueyo. "Fundamental limits to high-contrast wavefront control". In: *Techniques and Instrumentation for Detection of Exoplanets VIII*. Ed. by Stuart Shaklan. Vol. 10400. International Society for Optics and Photonics. SPIE, 2017, p. 1040014. DOI: 10.1117/12.2274657. URL: https://doi.org/10.1117/12.2274657.

[20] Eric Cady, Kunjithapatham Balasubramanian, Jessica Gersh-Range, Jeremy Kasdin, Brian Kern, Raymond Lam, Camilo Mejia Prada, Dwight Moody, Keith Patterson, Ilya Poberezhskiy, A. J. Eldorado Riggs, Byoung-Joon Seo, Fang Shi, Hong Tang, John Trauger, Hanying Zhou, and Neil Zimmerman. "Shaped pupil coronagraphy for WFIRST: high-contrast broadband testbed demonstration". In: *Techniques and Instrumentation for Detection of Exoplanets VIII*. Ed. by Stuart Shaklan. Vol. 10400. International Society for Optics and Photonics. SPIE, 2017, 104000E. DOI: 10.1117/12.2272834. URL: https://doi.org/10.1117/12.2272834.

[21] Sarah Tuttle, Mark Matsumura, David R. Ardila, Pin Chen, Michael Davis, Camden Ertley, Emily Farr, Brian Fleming, Kevin France, Cynthia Froning, Fabien Grisé, Erika Hamden, John Hennessy, Keri Hoadley, Stephan R. McCandliss, Drew M. Miles, Shouleh Nikzad, Manuel Quijada, Isu Ravi, Luis Rodriguez de Marcos, Paul Scowen, Oswald Siegmund, Carlos J. Vargas, Dmitry Vorobiev, and Emily M. Witt. *Ultraviolet Technology To Prepare For The Habitable Worlds Observatory*. 2024. arXiv: 2408.07242 [astro-ph.IM]. URL: https://arxiv.org/abs/2408.07242.

[22] Pin Chen, Laurent A. Pueyo, and Nicholas Siegler. "A coronagraph technology roadmap for future space observatories to directly image Earth-like exoplanets". In: *Space Telescopes and Instrumentation 2024: Optical, Infrared, and Millimeter Wave*. Ed. by Laura E. Coyle, Shuji Matsuura, and Marshall D. Perrin. Vol. 13092. International Society for Optics and Photonics. SPIE, 2024, 130921J. DOI: 10.1117/12.3018022. URL: https://doi.org/10.1117/12.3018022.

[23] Kyle Van Gorkom et al. *Performance predictions and contrast limits for an ultraviolet high contrast imaging testbed*. Accepted for publication in JATIS.

[24] James B. Breckinridge, Wai Sze T. Lam, and Russell A. Chipman. "Polarization Aberrations in Astronomical Telescopes: The Point Spread Function". In: *Publications of the Astronomical Society of the Pacific* 127.951 (2015), p. 445. DOI: 10.1086/681280. URL: https://dx.doi.org/10.1086/681280.

[25] Christopher B. Mendillo, Glenn A. Howe, Kuravi Hewawasam, Jason Martel, Timothy A. Cook, and Supriya Chakrabarti. "Polarization aberration analysis for the PICTURE-C exoplanetary coronagraph". In: *Journal of Astronomical Telescopes, Instruments, and Systems* 5.2 (2019), p. 025003. DOI: 10.1117/1.JATIS.5.2.025003. URL: https://doi.org/10.1117/1.JATIS.5.2.025003.

[26] Anche, Ramya M., Ashcraft, Jaren N., Haffert, Sebastiaan Y., Millar-Blanchaer, Maxwell A., Douglas, Ewan S., Snik, Frans, Williams, Grant, van Holstein, Rob G., Doelman, David, Van Gorkom, Kyle, and Skidmore, Warren. "Polarization aberrations in next-generation giant segmented mirror telescopes (GSMTs) - I. Effect on the coronagraphic performance". In: *A&A* 672 (2023), A121. DOI: 10.1051/0004-6361/202245651. URL: https://doi.org/10.1051/0004-6361/202245651.

[27] Christopher B. Mendillo, Glenn A. Howe, Kuravi Hewawasam, Jason Martel, Susanna C. Finn, Timothy A. Cook, and Supriya Chakrabarti. "Optical tolerances for the PICTURE-C mission: error budget for electric field conjugation, beam walk, surface scatter, and polarization aberration". In: *Techniques and Instrumentation for Detection of Exoplanets VIII*. Ed. by Stuart Shaklan. Vol. 10400. International Society for Optics and Photonics. SPIE, 2017, p. 1040010. DOI: 10.1117/12.2274105. URL: https://doi.org/10.1117/12.2274105.

[28] Garreth Ruane, Daniel Echeverri, Eduardo Bendek, Brian D. Kern, David Marx, Dimitri Mawet, Camilo Mejia Prada, A. J. Eldorado Riggs, Byoung-Joon Seo, Eugene Serabyn, and Stuart Shaklan. "Microelectromechanical deformable mirror development for high-contrast imaging, part 2: the impact of quantization errors on coronagraph image contrast". en. In: *Journal of Astronomical Telescopes, Instruments, and Systems* 6.04 (Oct. 2020). ISSN: 2329-4124. DOI: 10.1117/1.JATIS.6.4.045002. (Visited on 07/09/2021).

[29] Eduardo A. Bendek, Garreth J. Ruane, Camilo Mejia Prada, Christopher B. Mendillo, A.J. Eldorado Riggs, and Eugene Serabyn. "Microelectromechanical deformable mirror development for high-contrast imaging, part 1: miniaturized, flight-capable control electronics". In: *Journal of Astronomical Telescopes, Instruments, and Systems* 6.4 (2020), p. 045001. DOI: 10.1117/1.JATIS.6.4.045001. URL: https://doi.org/10.1117/1.JATIS.6.4.045001.

[30] Kyle Van Gorkom, Jared R. Males, Laird M. Close, Jennifer Lumbres, Alex D. Hedglen, Joseph D. Long, Sebastiaan Y. Haffert, Olivier Guyon, Maggie Y. Kautz, Lauren Schatz, Kelsey L. Miller, Alexander T. Rodack, Justin M. Knight, and Katie M. Morzinski. "Characterizing deformable mirrors for the MagAO-X instrument". In: *Journal of Astronomical Telescopes, Instruments, and Systems* 7.3 (2021), p. 039001. DOI:

10.1117/1.JATIS.7.3.039001. URL: https://doi.org/10.1117/1.JATIS.7.3.039001.

[31] Thomas E. Brooks and H. Philip Stahl. "Precision thermal control technology to enable thermally stable telescopes". In: *Journal of Astronomical Telescopes, Instruments, and Systems* 8 (2 2022).

[32] Christopher B. Mendillo, Joshua Brown, Jason Martel, Glenn A. Howe, Kuravi Hewawasam, Susanna C. Finn, Timothy A. Cook, Supriya Chakrabarti, Ewan S. Douglas, Dimitri Mawet, Olivier Guyon, Garima Singh, Julien Lozi, Kerri L. Cahoy, and Anne D. Marinan. "The low-order wavefront sensor for the PICTURE-C mission". In: *Techniques and Instrumentation for Detection of Exoplanets VII*. Ed. by Stuart Shaklan. Vol. 9605. International Society for Optics and Photonics. SPIE, 2015, p. 960519. DOI: 10.1117/12.2188238. URL: https://doi.org/10.1117/12.2188238.

[33] Garreth Ruane, Dimitri Mawet, Jeffrey Jewell, and Stuart Shaklan. "Performance and sensitivity of vortex coronagraphs on segmented space telescopes". In: *Techniques and Instrumentation for Detection of Exoplanets VIII*. Vol. 10400. SPIE, Sept. 2017, pp. 140–155. DOI: 10.1117/12.2274508. URL: https://www-spiedigitallibrary-org.ezproxy1.library.arizona.edu/conference-proceedings-of-spie/10400/104000J/Performance-and-sensitivity-of-vortex-coronagraphs-on-segmented-space-telescopes/10.1117/12.2274508.full (visited on 11/07/2021).

[34] Kunjithapatham Balasubramanian, A. J. Eldorado Riggs, Eric Cady, Victor White, Karl Yee, Daniel Wilson, Pierre Echternach, Richard Muller, Camilo Mejia Prada, Byoung-Joon Seo, Fang Shi, Daniel Ryan, Santos Fregoso, Jacob Metzman, and Robert Casey Wilson. "Fabrication of coronagraph masks and laboratory scale star-shade masks: characteristics, defects, and performance". In: *Techniques and Instrumentation for Detection of Exoplanets VIII*. Ed. by Stuart Shaklan. Vol. 10400. International Society for Optics and Photonics. SPIE, 2017, p. 104000C. DOI: 10.1117/12.2274059. URL: https://doi.org/10.1117/12.2274059.

[35] Amanda J. White and David M. Harrington. "Understanding polarization accuracy: the effect of mirror coating non-uniformity on instrument polarization". In: *Advances in Optical and Mechanical Technologies for Telescopes and Instrumentation V*. Ed. by Ramón Navarro and Roland Geyl. Vol. 12188. International Society for Optics and Photonics. SPIE, 2022, 121881R. DOI: 10.1117/12.2630684. URL: https://doi.org/10.1117/12.2630684.

[36] Matthew Noyes, Alex B. Walter, Greg Allan, Garreth Ruane, Eduardo Bendek, Phillip K. Poon, Camilo Meija Prada, A.J. El Dorado Riggs, Hong Tang, and Seth Meeker. "The decadal survey testbed two: a technology development facility for future exo-Earth observatories". In: *Techniques and Instrumentation for Detection of Exoplanets XI*. Ed. by Garreth J. Ruane. Vol. 12680. International Society for Optics and Photonics. SPIE, 2023, p. 1268017. DOI: 10.1117/12.2676452. URL: https://doi.org/10.1117/12.2676452.

[37] Russell A Chipman, Wai-Sze Tiffany Lam, and Garam Young. *Polarized light and optical systems*. CRC press, 2018.

[38] Stuart B. Shaklan and Joseph J. Green. "Reflectivity and optical surface height requirements in a broadband coronagraph. 1.Contrast floor due to controllable spatial frequencies". In: *Appl. Opt.* 45.21 (2006), pp. 5143–5153. DOI: 10.1364/AO.45.005143. URL: https://opg.optica.org/ao/abstract.cfm?URI=ao-45-21-5143.

[39] Laurent Pueyo and N. Jeremy Kasdin. "Polychromatic Compensation of Propagated Aberrations for High-Contrast Imaging". en. In: *The Astrophysical Journal* 666.1 (Sept. 2007), pp. 609–625. ISSN: 0004-637X, 1538-4357. DOI: 10.1086/518884. URL: https://iopscience.iop.org/article/10.1086/518884 (visited on 07/09/2021).

[40] Amir Give'on, N. Jeremy Kasdin, Robert J. Vanderbei, and Yoav Avitzour. "On representing and correcting wavefront errors in high-contrast imaging systems". In: *J. Opt. Soc. Am. A* 23.5 (2006), pp. 1063–1073. DOI: 10.1364/JOSAA.23.001063. URL: https://opg.optica.org/josaa/abstract.cfm?URI=josaa-23-5-1063.

[41] E. Sidick, S. Shaklan, K. Balasubramanian, and E. Cady. "High-contrast coronagraph performance in the presence of focal plane mask defects". In: *Society of Photo-Optical Instrumentation Engineers (SPIE) Conference Series*. Vol. 9143. Society of Photo-Optical Instrumentation Engineers (SPIE) Conference Series. Aug. 2014, 914336, p. 36. DOI: 10.1117/12.2055004.

[42] K. Dohlen. "Aspects of error budgeting for coronagraphic differential imaging: effects of dust and cosmetic errors". In: *Society of Photo-Optical Instrumentation Engineers (SPIE) Conference Series*. Vol. 7017. Society of Photo-Optical Instrumentation Engineers (SPIE) Conference Series. July 2008, 70171V, p. 1. DOI: 10.1117/12.789935.

[43] K. Balasubramanian, S. Shaklan, and A. Give'On. "Stellar coronagraph performance impact due to particulate contamination and scatter". In: *Society of Photo-Optical Instrumentation Engineers (SPIE) Conference Series*. Vol. 7440. Society of Photo-Optical Instrumentation Engineers (SPIE) Conference Series. Aug. 2009, 74400T, p. 0. DOI: 10.1117/12.825182.

[44] E. L. Church, P. Z. Takacs, and T. A. Leonard. "The Prediction Of BRDFs From Surface Profile Measurements". In: *Scatter from Optical Components*. Ed. by J. C. Stover. Vol. 1165. Society of Photo-Optical Instrumentation Engineers (SPIE) Conference Series. Jan. 1990, pp. 136–150. DOI: 10.1117/12.962842.

[45] John. C. Stover. *Optical Scattering: Measurement and Analysis*. 3rd ed. SPIE, 1995. DOI: 10.1117/3.203079. URL: http://ebooks.spiedigitallibrary.org/book.aspx?bookid=203.

[46] J. M. Elson and J. M. Bennett. "Calculation of the power spectral density from surface profile data". In: *Applied optics* 34 (Jan. 1995), pp. 201–208. DOI: 10.1364/AO.34.000201.

[47] Michael G Dittman. "K-correlation power spectral density and surface scatter model". In: *Optical Systems Degradation, Contamination, and Stray Light: Effects, Measurements, and Control II*. Vol. 6291. SPIE. 2006, pp. 226–237.

[48] James E Harvey, Andrey Krywonos, and John C Stover. "Unified scatter model for rough surfaces at large incident and scatter angles". In: *Advanced Characterization Techniques for Optics, Semiconductors, and Nanotechnologies III*. Vol. 6672. SPIE. 2007, pp. 103–110.

[49] Peter G Nelson. "An analysis of scattered light in reflecting and refracting primary objectives for coronagraphs". In: *Coronal Solar Magnetism Observatory Technical Note* 4 (2007), pp. 10–06.

[50] James E Harvey, Narak Choi, Andrey Krywonos, and Jesus Grasa Marcen. "Calculating BRDFs from surface PSDs for moderately rough optical surfaces". In: *Optical Manufacturing and Testing VIII*. Vol. 7426. SPIE. 2009, pp. 141–149.

[51] A. Krywonos, J. E. Harvey, and N. Choi. "Linear systems formulation of scattering theory for rough surfaces with arbitrary incident and scattering angles". In: *Journal of the Optical Society of America A* 28 (June 2011), p. 1121. DOI: 10.1364/JOSAA.28.001121.

[52] J. E. Harvey, S. Schröder, N. Choi, and A. Duparré. "Total integrated scatter from surfaces with arbitrary roughness, correlation widths, and incident angles". In: *Optical Engineering* 51.1 (Jan. 2012), pp. 013402–013402. DOI: 10.1117/1.OE.51.1.013402.

[53] Hashima Hasan and C. J. Burrows. "TELESCOPE IMAGE MODELLING (TIM)". In: *Publications of the Astronomical Society of the Pacific* 107.709 (1995), p. 289. DOI: 10.1086/133552. URL: https://dx.doi.org/10.1086/133552.

[54] Christian Marois, Bruce Macintosh, Rémi Soummer, Lisa Poyneer, and Brian Bauman. "An end-to-end polychromatic Fresnel propagation model of GPI". In: *Adaptive Optics Systems*. Ed. by Norbert Hubin, Claire E. Max, and Peter L. Wizinowich. Vol. 7015. International Society for Optics and Photonics. SPIE, 2008, 70151T. DOI: 10.1117/12.789899. URL: https://doi.org/10.1117/12.789899.

[55] Olivier Guyon, Eugene A. Pluzhnik, Raphael Galicher, Frantz Martinache, Stephen T. Ridgway, and Robert A. Woodruff. "Exoplanet Imaging with a Phase-induced Amplitude Apodization Coronagraph. I. Principle". In: *The Astrophysical Journal* 622.1 (2005), p. 744. DOI: 10.1086/427771. URL: https://dx.doi.org/10.1086/427771.

[56] Kyle Van Gorkom, Ewan S. Douglas, Kian Milani, Jaren N. Ashcraft, Ramya M. Anche, Emory Jenkins, Patrick Ingraham, Sebastiaan Haffert, Daewook Kim, Heejoo Choi, and Olivier Durney. "The space coronagraph optical bench (SCoOB): 4. Vacuum performance of a high contrast imaging testbed". In: *Space Telescopes and Instrumentation 2024: Optical, Infrared, and Millimeter Wave*. Ed. by Laura E. Coyle, Shuji Matsuura, and Marshall D. Perrin. Vol. 13092. International Society for Optics and Photonics. SPIE, 2024, p. 1309222. DOI: 10.1117/12.3020654. URL: https://doi.org/10.1117/12.3020654.

[57] Emory L. Jenkins, Kyle Van Gorkom, Kevin Derby, Patrick Ingraham, and Ewan S. Douglas. "Microfabricated pinholes for high contrast imaging testbeds". In: *Techniques and Instrumentation for Detection of Exoplanets XI*. Ed. by Garreth J. Ruane. Vol. 12680. International Society for Optics and Photonics. SPIE, 2023, 126801A. DOI: 10.1117/12.2677630. URL: https://doi.org/10.1117/12.2677630.

[58] *Metachrome UV-Conversion Coatings*. URL: https://www.actonoptics.com/en-us/products/metachrome-uv-conversion-coatings-for-sensors.

[59] Rémi Soummer, Gregory R. Brady, Keira Brooks, Thomas Comeau, Élodie Choquet, Tom Dillon, Sylvain Egron, Rob Gontrum, John Hagopian, Iva Laginja, Lucie Leboulleux, Marshall D. Perrin, Peter Petrone, Laurent Pueyo, Johan Mazoyer, Mamadou N'Diaye, A. J. Eldorado Riggs, Ron Shiri, Anand Sivaramakrishnan, Kathryn St. Laurent, Ana-Maria Valenzuela, and Neil T. Zimmerman. "High-contrast imager for complex aperture telescopes (HiCAT): 5. first results with segmented-aperture coronagraph and wavefront control". In: *Space Telescopes and Instrumentation 2018: Optical, Infrared, and Millimeter Wave*. Ed. by Makenzie Lystrup, Howard A. MacEwen, Giovanni G. Fazio, Natalie Batalha, Nicholas Siegler, and Edward C. Tong. Vol. 10698. International Society for Optics and Photonics. SPIE, 2018, 106981O. DOI: 10.1117/12.2314110. URL: https://doi.org/10.1117/12.2314110.

[60] John G. Hagopian, Stephanie A. Getty, Manuel Quijada, June Tveekrem, Ron Shiri, Patrick Roman, James Butler, Georgi Georgiev, Jeff Livas, Cleophus Hunt, Alejandro Maldonado, Saikat Talapatra, Xianfeng Zhang, Stergios J. Papadakis, Andrew H. Monica, and David Deglau. "Multiwalled carbon nanotubes for stray light suppression in space flight instruments". In: *Carbon Nanotubes, Graphene, and Associated Devices III*. Ed. by Didier Pribat, Young-Hee Lee, and Manijeh Razeghi. Vol. 7761. International Society for Optics and Photonics. SPIE, 2010, 77610F. DOI: 10.1117/12.864386. URL: https://doi.org/10.1117/12.864386.

[61] Emiel H. Por, Sebastiaan Y. Haffert, Vikram M. Radhakrishnan, David S. Doelman, Maaike van Kooten, and Steven P. Bos. "High Contrast Imaging for Python (HCIPy): an open-source adaptive optics and coronagraph simulator". In: *Adaptive Optics Systems VI*. Ed. by Laird M. Close, Laura Schreiber, and Dirk Schmidt. Vol. 10703. International Society for Optics and Photonics. SPIE, 2018, p. 1070342. DOI: 10.1117/12.2314407. URL: https://doi.org/10.1117/12.2314407.

[62] Amber V. Young, Tyler D. Robinson, Joshua Krissansen-Totton, Edward W. Schwieterman, Nicholas F. Wogan, Michael J. Way, Linda E. Sohl, Giada N. Arney, Christopher T. Reinhard, Michael R. Line, David C. Catling, and James D. Windsor. "Inferring Chemical Disequilibrium Biosignatures for Proterozoic Earth-Like Exoplanets". In: *arXiv e-prints*, arXiv:2311.06083 (Nov. 2023), arXiv:2311.06083. DOI: 10.48550/arXiv.2311.06083. arXiv: 2311.06083 [astro-ph.EP].

[63] Tyler D. Robinson and Arnaud Salvador. "Exploring and Validating Exoplanet Atmospheric Retrievals with Solar System Analog Observations". In: PSJ 4.1, 10 (Jan. 2023), p. 10. DOI: 10.3847/PSJ/acac9a. arXiv: 2204.04231 [astro-ph.EP].

[64] Garreth Ruane, A. J. Eldorado Riggs, Eugene Serabyn, Wesley Baxter, Camilo Mejia Prada, Dimitri Mawet, Matthew Noyes, Phillip K. Poon, and Nelson Tabiryan. "Broadband vector vortex coronagraph testing at NASA's high contrast imaging testbed facility". In: *Space Telescopes and Instrumentation 2022: Optical, Infrared, and Millimeter Wave*. Vol. 12180. SPIE, Aug. 2022, pp. 793–806. DOI: 10.1117/12.2628972. URL: https://www.spiedigitallibrary.org/conference-proceedings-of-spie/

12180/1218024/Broadband-vector-vortex-coronagraph-testing-at-NASAs-high-contrast-imaging/10.1117/12.2628972.full (visited on 02/08/2023).

[65] Jaren N Ashcraft, Ewan S Douglas, Ramya M Anche, Kyle Van Gorkom, Emory Jenkins, William Melby, and Maxwell A Millar-Blanchaer. "The space coronagraph optical bench (SCoOB): 3. Mueller matrix polarimetry of a coronagraphic exit pupil". In: *Space Telescopes and Instrumentation 2024: Optical, Infrared, and Millimeter Wave*. Vol. 13092. SPIE. 2024, pp. 2117–2132.

[66] A. J. Eldorado Riggs, Garreth Ruane, Camilo A. Mejia Prada, David S. Marx, and Byoung-Joon Seo. "High contrast imaging with MEMS deformable mirrors in the Decadal Survey Testbed". In: *Techniques and Instrumentation for Detection of Exoplanets X*. Vol. 11823. SPIE, Sept. 2021, pp. 259–267. DOI: 10.1117/12.2593459. URL: https://www.spiedigitallibrary.org/conference-proceedings-of-spie/11823/118230S/High-contrast-imaging-with-MEMS-deformable-mirrors-in-the-Decadal/10.1117/12.2593459.full (visited on 02/08/2023).

[67] Jorge Llop-Sayson, Garreth Ruane, Dimitri Mawet, Nemanja Jovanovic, Carl T. Coker, Jacques-Robert Delorme, Daniel Echeverri, Jason Fucik, A. J. Eldorado Riggs, and J. Kent Wallace. "High-contrast Demonstration of an Apodized Vortex Coronagraph". en. In: *The Astronomical Journal* 159.3 (Feb. 2020). Publisher: The American Astronomical Society, p. 79. ISSN: 1538-3881. DOI: 10.3847/1538-3881/ab6329. URL: https://dx.doi.org/10.3847/1538-3881/ab6329 (visited on 02/08/2023).

[68] E. Serabyn, J. Trauger, D. Moody, D. Mawet, K. Liewer, J. Krist, and B. Kern. "High-contrast imaging results with the vortex coronagraph". In: *Techniques and Instrumentation for Detection of Exoplanets VI*. Vol. 8864. SPIE, Sept. 2013, pp. 361–366. DOI: 10.1117/12.2024660. URL: https://www.spiedigitallibrary.org/conference-proceedings-of-spie/8864/88640Y/High-contrast-imaging-results-with-the-vortex-coronagraph/10.1117/12.2024660.full (visited on 02/08/2023).

[69] Camilo Mejia Prada, Eugene Serabyn, and Fang Shi. "High-contrast imaging stability using MEMS deformable mirror". In: *Techniques and Instrumentation for Detection of Exoplanets IX*. Vol. 11117. SPIE, Sept. 2019, pp. 112–118. DOI: 10.1117/12.2525628. URL: https://www.spiedigitallibrary.org/conference-proceedings-of-spie/11117/1111709/High-contrast-imaging-stability-using-MEMS-deformable-mirror/10.1117/12.2525628.full (visited on 02/08/2023).

[70] Garreth Ruane, Eugene Serabyn, Camilo Mejia Prada, Wesley Baxter, Eduardo Bendek, Dimitri Mawet, and A. J. Eldorado Riggs. "Experimental analysis of the achromatic performance of a vector vortex coronagraph". In: *Space Telescopes and Instrumentation 2020: Optical, Infrared, and Millimeter Wave*. Vol. 11443. SPIE, Dec. 2020, pp. 504–516. DOI: 10.1117/12.2561593. URL: https://www.spiedigitallibrary.org/conference-proceedings-of-spie/11443/1144320/Experimental-analysis-of-the-achromatic-performance-of-a-vector-vortex/10.1117/12.2561593.full (visited on 02/08/2023).

[71] Christopher B. Mendillo, Kuravi Hewawasam, Jason Martel, Thaddeus Potter, Timothy A. Cook, and Supriya Chakrabarti. "The PICTURE-C exoplanetary imaging balloon mission: laboratory coronagraph demonstrations of high-contrast imaging and low-order wavefront control". In: *Space Telescopes and Instrumentation 2022: Optical, Infrared, and Millimeter Wave*. Vol. 12180. SPIE, Aug. 2022, pp. 776–785. DOI: 10.1117/12.2630237. URL: https://www.spiedigitallibrary.org/conference-proceedings-of-spie/12180/1218022/The-PICTURE-C-exoplanetary-imaging-balloon-mission--laboratory-coronagraph/10.1117/12.2630237.full (visited on 02/08/2023).

[72] Russell A. Chipman and Shih-Yau Lu. "Decomposition of Mueller matrices". In: *Wideband Interferometric Sensing and Imaging Polarimetry*. Ed. by Harold Mott and Wolfgang-Martin Boerner. Vol. 3120. International Society for Optics and Photonics. SPIE, 1997, pp. 385 –396. DOI: 10.1117/12.283849. URL: https://doi.org/10.1117/12.283849.